Unconventional magnetic states and defects

Barts, Evgenii

DOI:
10.33612/diss.784926551

Chapter 2

Magnetostatic Skyrmion bubbles in strongly anisotropic ferromagnetic thin films

Abstract

Topological magnetic bubbles, called skyrmions, are widely observed and studied in chiral magnets, where they are stabilized by Dzyaloshinskii-Moriya interaction. We discuss skyrmions stabilized by magnetostatic interactions in centrosymmetric ferromagnetic thin films. We use realistic model parameters for a relatively thick film of itinerant $SrRuO_3$ ferromagnet. In this material, hump features were observed in an off-diagonal Hall response[1] ascribed to the Topological Hall effect caused by stable skyrmion lattices in an intermediate magnetic field region. We numerically show that magnetostatic interactions are the main mechanism stabilizing the topological magnetic bubbles in these centrosymmetric magnets with no heavy metal interfaces. The experimentally observed robustness of the skyrmion lattices against oblique magnetic fields is related to higher-order magnetocrystalline anisotropy of Ru ions with strong spin-orbit coupling.

2.1 Introduction

Magnetic bubbles, small domains of magnetization-down inside the homogeneous magnetization-up ground state, served as information carriers in the first kind of magnetic memory devices (see Chapter 1 for detail). In-plane spins in the cylindrical domain wall surrounding the magnetic bubble can form a vortex texture giving skyrmion topology to the bubble. If all spins in the skyrmion emanated from a single point, they would wrap a sphere around precisely once. Skyrmions recently found in chiral magnets hold the promise of high-density magnetic memory devices [36, 58]. The lack of inversion symmetry in chiral magnets allows for Dzyaloshinskii-Moriya (DM) asymmetric exchange interactions favoring non-collinear spin textures.

[1] P. Zhang, A. Das, E. Barts, M. Azhar, L. Si, K. Held, M. Mostovoy, and T. Banerjee. Robust skyrmion-bubble textures in $SrRuO_3$ thin films stabilized by magnetic anisotropy *Phys. Rev. Research* **2**, 032026(R) (2020)

Skyrmions show significant stability and high mobility compared to domain walls, and can have a tiny size, which are essential for applications in novel computing and data storage devices. Remarkably skyrmion acts as a quantized magnetic field flux on conduction electrons [2]. In electron transport measurements, this effect results in enhanced off-diagonal resistivity, coined Topological Hall effect (THE). It is one of the techniques to detect and study skyrmions in bulk chiral magnets and multilayers of conventional magnets with heavy-metal materials [36, 59–62].

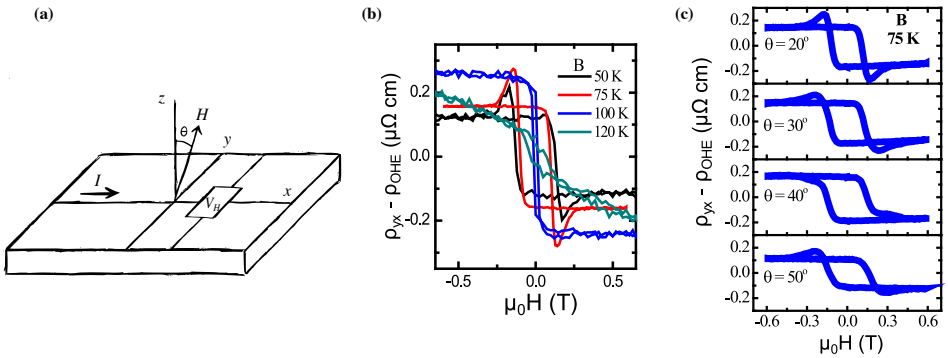

Figure 2.1: ***Summary of experimental results*** *with (a) the schematic setup for Hall effect measurements. The off-diagonal resistivity is measured with a potential drop, V_H along y direction at electric current along x direction. The magnetic field is applied in the orthogonal z direction with a possible inclination angle θ. (b) The experimentally measured off-diagonal resistivity is plotted versus applied field H at various temperatures and (c) magnetic field tilting angles. The figures (b) and (c) are from Ref. [63].*

Our experimental collaborators observed the THE in thin films of conducting $SrRuO_3$ with thickness varying from 7 to 10 nm [63]. In the case of the bulk single crystal, Ru^{2+} $4d$ ions form orthorhombic lattice showing ferromagnetic order at temperatures below 150-160 K with the magnetic moment of 1.4-2.0 μ_B per Ru ion [64]. The anomalous electron transport properties of this material have been under scrutiny for decades [65–67]

We focus on ferromagnetic thin films with the ordering temperature of 120K and with the much larger saturation magnetic moment of $\approx 3\mu_B$ per Ru ion [63]. Unique to this study of the conducting oxides is the robustness of the hump signatures in off-diagonal resistivity to the tilts of magnetic field and temperature (see Fig. 2.1). Such features were attributed to the THE in the case of ultrathin films of $SrRuO_3$ grown on the substrate of $SrIrO_3$ [68, 69]. Direct imaging of a skyrmion with the size of approximately 10 nm was done by magnetic force microscopy [70]. In contrast, we have no interface with a heavy-metal layer, such as one with Ir ions. Hence, an induced interfacial DM interaction cannot be the primary mechanism of skyrmion

stability for the relatively thick films of the centrosymmetric $SrRuO_3$ grown on the $SrTiO_3$ substrate.

We show that the often ignored long-range magnetodipolar interaction plays a key role in skyrmion stabilization at intermediate film thicknesses. In addition, we invoke the higher-order magnetocrystalline anisotropy of heavy Ru cations that boosts the stability of skyrmions in oblique magnetic fields. We show that the skyrmion crystals induced by magnetostatic interactions have a much greater stability region than it was previously considered. Our numerical method allows us to optimize the shape of skyrmions forming the crystal, in contrast to the Kooy-Enz model of magnetic bubbles with sharp boundaries [71]. Combining gradient and non-gradient energy optimizations, we compare energies of the competing magnetic phases under applied magnetic fields for various strengths of single-ion anisotropy and the field inclinations, which allows us to construct detailed phase diagrams of these materials. These new insights explain the origin of the observed THE and the higher skyrmion stability.

2.2 Magnetic model

To cast light on the robust THE signals, we examine the stability of the magnetic bubble array in thin films with the energy given by

$$\begin{aligned} E = h \int d^2x \Big[\sum_{i=x,y} \frac{c}{2} (\partial_i \boldsymbol{M})^2 - \frac{K_1}{2} M_z^2 - \frac{K_2}{4M_\mathrm{s}^2} M_z^4 \\ - \boldsymbol{H} \cdot \boldsymbol{M} + \frac{\lambda}{4M_\mathrm{s}^2} \left(\boldsymbol{M}^2 - M_\mathrm{s}^2 \right)^2 \Big] + E_\mathrm{ms}, \end{aligned} \tag{2.1}$$

in which we assumed for simplicity the magnetization vector to be independent of the vertical coordinate, z: $\boldsymbol{M} = \boldsymbol{M}(x, y)$.

The first energy term is the exchange energy, the second and third terms are the orthorhombic magnetocrystalline anisotropy energies of the second and fourth-order, respectively, and the fourth term is the Zeeman energy (in CGS units). We use the fifth term in Eq. (2.1) with the parameter $\lambda = 100$ to constrain the magnitude of the magnetization to its saturation value, $\boldsymbol{M} = M_\mathrm{s}\boldsymbol{m}$ ($\boldsymbol{m}^2 = 1$). The magnetostatic energy, E_ms, has compact form in the reciprocal space [34] (see Introduction Sec. 1.3 for details).

Figure 2.2 shows noncollinear magnetic states stabilized by magnetostatic interactions and an applied magnetic field: a triangular array of Bloch skyrmions (type-I bubbles) with the topological charge -1 in real space (panel a) and in the reciprocal space (panel d), an array of type II bubbles with zero topological charge favored by tilted magnetic fields (panel b) and the stripe domain state appearing in weak applied fields (panel c). The configurations are obtained by minimizing energy Eq. (2.1) on

the space of 61 Fourier harmonics of the magnetization, which is sufficient to describe the skyrmion lattice (see Appendix 2.6.1 for details of simulations).

Earlier studies of relatively thick films suggested that stability of the stripe domain state and bubble array requires the quality factor, $Q = \frac{K_1}{4\pi} > 1$ [32, 33, 71]. For $Q < 1$, the perpendicular magnetic anisotropy is not strong enough to overcome magnetostatic interactions favoring a uniform state with in-plane magnetization. However, recent micromagnetic simulations of thin films showed that inhomogeneous magnetic states could be induced by an applied magnetic field even for $Q < 1$ [72]. This is partly related to the fact that in thin films, the domain wall width is no longer negligibly small compared to the film thickness, as can be seen from Fig. 2.2. In addition, the notion of an effective magnetic anisotropy, $K_{\text{eff}} = K_1 - 4\pi$, is only meaningful for uniform states since dipole-dipole interactions strongly depend on the magnetic modulation wave vector.

Moreover, the phase diagram in Fig. 2.3a,b calculated for the magnetic field normal to the film shows that the field interval in which the skyrmion crystal (SkX) has the lowest energy widens as the quality factor decreases. The SkX becomes unstable for $Q \lesssim 0.75$, near the line separating the uniform states with the perpendicular (white color) and tilted (red color) magnetization. The stability region of the SkX phase extends to lower Q and higher critical fields when we include the 4^{th}-order magnetocrystalline anisotropy, which is relatively large in SRO due to the strong spin-orbit coupling of Ru [73, 74]. Figure 2.3b shows the phase diagram calculated for $R = \frac{K_2}{4\pi} = 0.4$. $R > 0$ favors magnetization normal to the film, which makes the SkX more stable. Thus, a smaller quality factor in combination with a higher-order anisotropy can significantly increase the stability of the SkX. Although, the fields at which the SkX undergoes the transition into a uniform state are still two to three times lower than the field of ~ 400 mT at which THE disappears in the experiment. The magnetization relaxation along the z direction and finite-size effects [75] can further increase the stability of skyrmions.

2.3 Metastability of skyrmions

Isolated skyrmions can survive at much higher applied magnetic fields and provide THE in the metastable regime of the skyrmion lattice. We consider a two-parametric variational Ansatz of the isolated Bloch skyrmion,

$$1 - m_z(r) = \frac{2}{\left(1 + \left(\frac{r}{a}\right)^2\right)^{1+\epsilon}}, \tag{2.2}$$

where r is the distance from the bubble. In this Ansatz, the polar angle θ describing the profile of magnetization direction, $\boldsymbol{m} = (\cos\Phi\sin\theta, \sin\Phi\sin\theta, \cos\theta)^T$, only depends

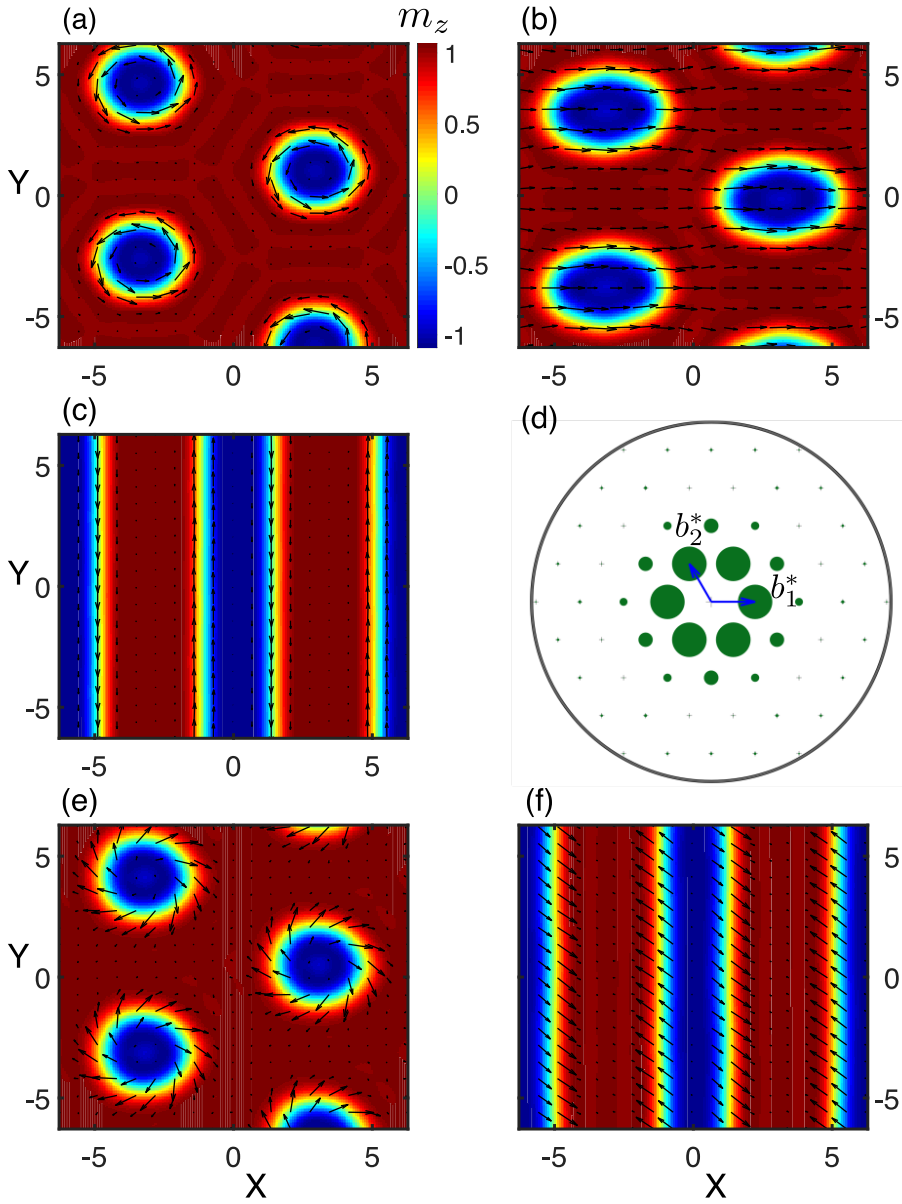

Figure 2.2: ***Competing non-collinear magnetic phases****: (a) an array of bubbles with topological charge −1, (b) an array of bubbles carrying zero topological charge and an in-plane magnetic moment, and (c) the stripe domain state. In-plane components of* $\boldsymbol{m}$ *are shown with arrows,* m_z *is color-coded. Distances are given in units of the film thickness,* h*. (d) Skyrmion crystal in reciprocal space (large zero harmonic is excluded for clarity). The green dot area is proportional to the magnitude of the Fourier harmonic of the magnetization. The black line encircles the subspace of 61 wave vectors. Effect of the interfacial Dzyaloshinskii-Moriya interaction,* $D = 1$*, on (e) skyrmions and (f) domain walls in the stripe domain state. Both acquire a Néel component.*

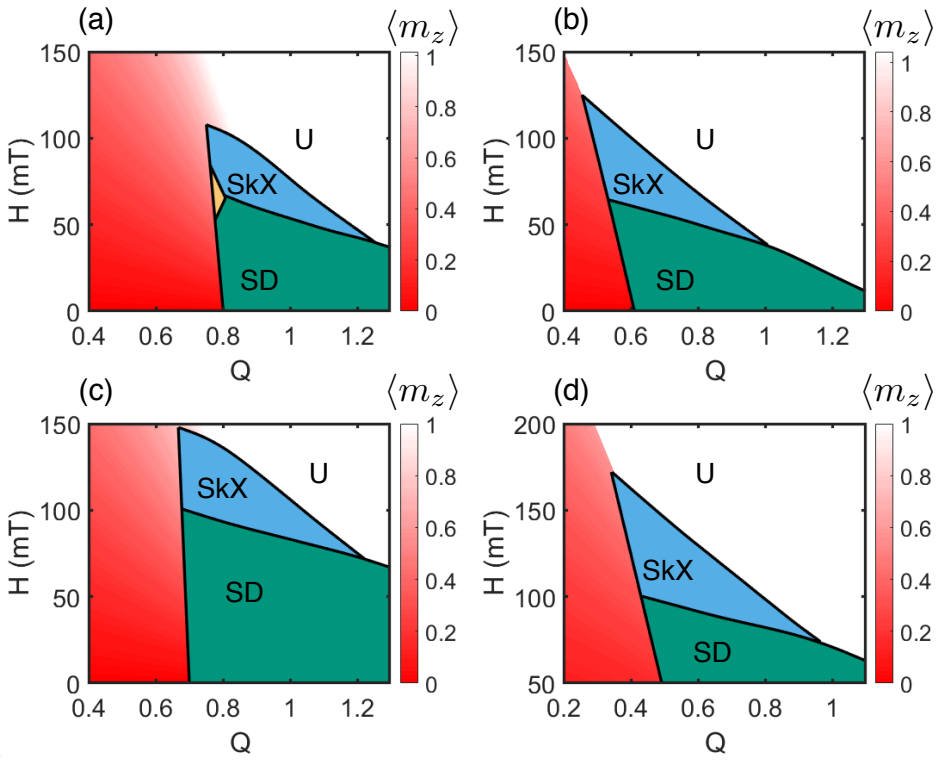

Figure 2.3: ***Phase diagrams*** *of magnetic field, H, vs quality factor, $Q = \frac{K_1}{4\pi}$, which include the skyrmion crystal (SkX), stripe domain (SD) and uniform (U) states. Red color intensity indicates m_z in the uniform state with a tilted magnetization. The state with the magnetization normal to the film is shown with white color. These diagrams are calculated for (a) $R = \frac{K_2}{4\pi} = 0$ and (b) $R = 0.4$. The interfacial DM interaction with $D = 1$ widens the regions occupied by the SkX and SD phases, calculated for (c) $R = 0$ and (d) $R = 0.4$.*

on r. The skyrmion is of Bloch type, $\Phi = \frac{\pi}{2} + \varphi$, with φ being azimuthal angle, which induces no bulk magnetic charges ($\sim \nabla \cdot \boldsymbol{m}$). Minimization of the bubble energy with respect to the variational parameters, a and ϵ, can be done semi-analytically by solving transcendental equations (details in Appendix 2.6.2).

Figures 2.4 a,b compares the upper critical field (the red curve) beyond which an isolated skyrmion becomes unstable with the critical field for skyrmion crystal (above the light blue region) as a function of the quality factor Q for $R = 0$ (and $R = 0.4$, respectively). The blue curve shows a similar upper critical field but with no minimization with respect to ϵ, for $\epsilon = 1/2$. The latter provides less accurate results but can be calculated fully analytically.

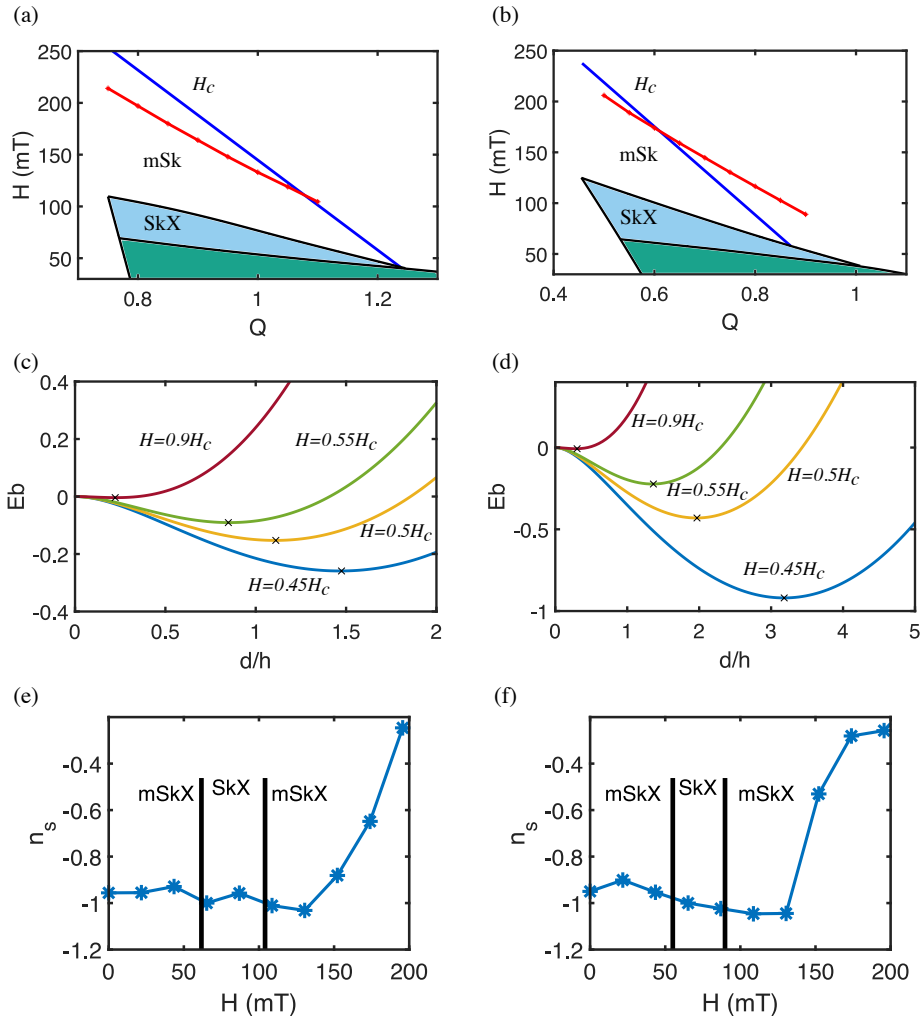

Figure 2.4: ***Metastable skyrmions***. *The red solid line shows the upper critical field for a single skyrmion against the quality factor Q obtained with variational solution for (a) $R = 0$ and (b) $R = 0.4$. The blue line shows the upper critical field calculated for the one parameter variational solution, for constant $\epsilon = 0.5$. For comparison, the phase diagram from Fig. 2.3 was partially drawn. The bubble energy (E_b) dependence on its size is shown for (c) $R = 0$ and (d) $R = 0.1$ and for various applied fields indicated by color. The bubble diameter ($d = 2a$) is rescaled with the film thickness, h. The skyrmion charge density of stable skyrmion crystals plotted versus magnetic fields for $R = 0$ and (e) $Q = 0.85$ (f) $Q = 0.95$.*

In the case of one-parametric variational ansatz ($\epsilon = 0.5$), the energy of the bubble is

$$E_{\text{bubble}} = \pi^2 M_{\text{s}}^2 h d^2 \left(3(Q-1) - \frac{87}{140\pi} K_2 + \frac{H}{\pi M_{\text{s}}} - \frac{h}{d+h} \right) + \text{const}, \tag{2.3}$$

where $d = 2a$ is the diameter of the skyrmion. Apart from numerical coefficients, which are calculated in Appendix 2.6.2, the size energy dependence can be understood using simple scaling arguments. The single-ion anisotropic interactions scale with the bubble area ($\sim d^2$). The exchange energy is not present since it is scale-invariant in two dimensions. The magnetostatic energy of the Bloch skyrmion,

$$E_{\text{ms}} = 2\pi h S \sum_{\boldsymbol{q}} f(qh) |M_{\boldsymbol{q}}^z|^2, \tag{2.4}$$

with $f(x) = \frac{1-e^{-x}}{x}$, scales linearly with the bubble diameter ($\sim d$), for $d \ll h$, and quadratically ($\sim d^2$) for $d \gg h$, as follows from the large-q and low-q expansion of the magnetostatic energy, respectively. This is due to the expansion of $f(x \gg 1) \approx \frac{1}{x}$ and $f(x \ll 1) \approx 1$. The critical field at which the bubble collapses is then given by

$$H_{\text{c}} = 4\pi M_{\text{s}} \left(1 - \frac{3}{4} Q + \frac{87}{140} R \right), \tag{2.5}$$

which is obtained by minimization of the bubble energy. The bubble energy size dependence is shown in Fig. 2.4c,d for various magnitudes of applied fields. The optimal bubble radius goes to zero as the field approaches its critical value.

Our numerical procedures are tailored to describe periodic states and are not efficient at studying gas of isolated skyrmions at high applied fields. Nevertheless, they predict that the skyrmion density should decrease with increasing the magnetic field, as shown in Fig. 2.4e,f.

2.4 Phase diagrams in oblique magnetic fields

In tilted magnetic fields (see Fig. 2.5a), the bubbles with skyrmion topology become unstable and transform into non-topological bubbles (NTB) with two Bloch points and an in-plane magnetic dipole moment (Fig. 2.2b), resulting in the disappearance of the THE. In the M-type hexaferrite with $Q \sim 1$, the topological phase disappears at a small tilt angle, $\theta = 2.3^\circ$ [34]. The THE found at much larger θ in our experiment can be explained by strong 4^{th}-order anisotropy (see Fig. 2.5b, c). The insets show angular dependence of the anisotropy energy in the uniform state as a function of the magnetization tilt angle, θ_{m}. As R increases, the anisotropy energy, in addition to the global minimum at $\theta_{\text{m}} = \pm\frac{\pi}{2}$ (in-plane magnetization), acquires a local minimum

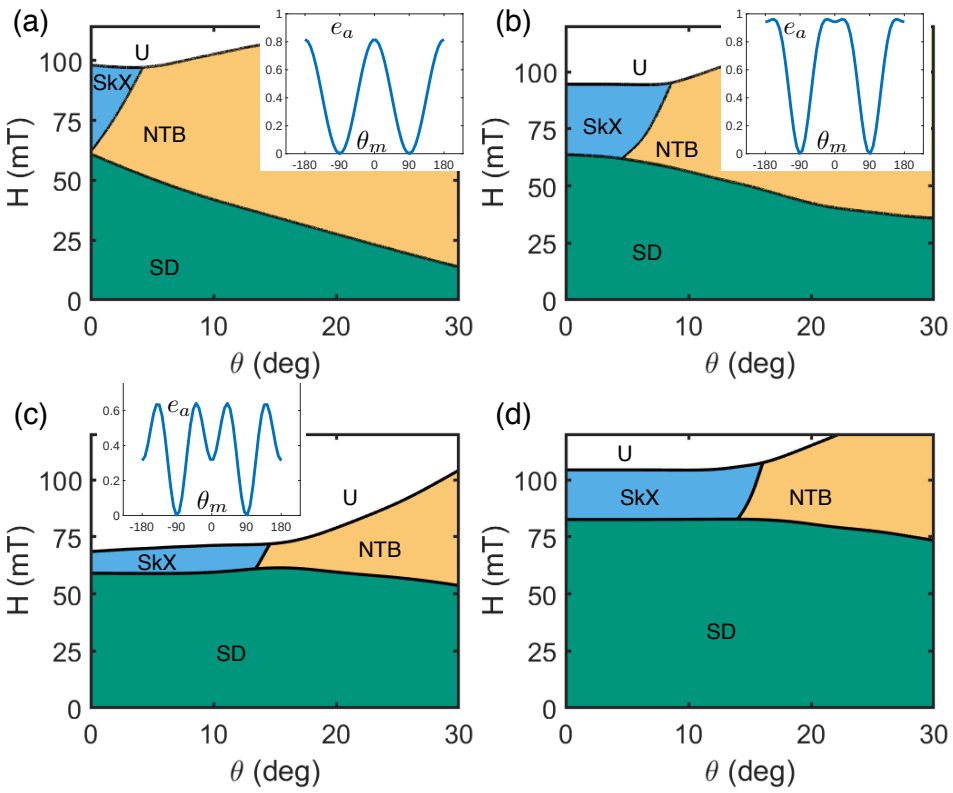

Figure 2.5: ***Phase diagrams in a tilted magnetic field***, *θ being the tilt angle, for (a) $Q = 0.87$ and $R = 0$, (b) $Q = 0.65$ and $R = 0.40$ and (c) $Q = 0.65$ and $R = 0.60$, and (d) $Q = 0.65, R = 0.60$ with additional $D = 1$. In addition to the skyrmion crystal (SkX, blue), stripe domain (SD, green) and uniform (U, white) states, these diagrams include an array of non-topological bubbles (NTB, yellow). The insets show the dependence of the dimensionless anisotropy energy density, e_a, in the uniform state on the magnetization tilt angle, θ_m, for the corresponding parameter sets.*

at $\theta_m = 0, \pi$ (out-of-plane magnetization), which leads to an increase of the field tilt angle θ, at which the THE disappears.

The interfacial Dzyaloshinskii-Moriya interaction,

$$E_{\mathrm{DM}} = Dh^2 \int d^2x \left[(\boldsymbol{M} \cdot \boldsymbol{\nabla}) M_z - M_z (\boldsymbol{\nabla} \cdot \boldsymbol{M}) \right], \tag{2.6}$$

is effectively small due to the large number of magnetic RuO_2-layers in the SRO films and the absence of heavy metal elements. Nevertheless, it can make skyrmions more resilient to high magnetic fields (see Figs. 2.3c, d), as they acquire a Néel component

(Fig. 2.2e, f). In addition, bubbles with skyrmion topology become more stable against the transition into non-topological bubbles in tilted magnetic fields, as shown in Figs. 2.5c, d.

2.5 Discussion

Our results support the skyrmionic scenario of experimentally observed THE signatures in $SrRuO_3$ films. The key trends discussed in this work are the importance of inhomogeneous magnetostatic energy, abandoned in previous discussions, in skyrmion stabilization in thin films at intermediate thicknesses ($\sim$ 10 nm) and the enhanced stability of skyrmions to inclined applied fields provided by the multiaxial anisotropy.

However, the actual observables of simulations with the realistic model parameters do not fully match the experimental data. The calculated critical fields are 2-3 times smaller, and critical angles are 2 times smaller on average compared to experimental values. We showed that the skyrmion crystals could survive in much higher fields in the metastable regime. Temperature fluctuations, neglected in our discussion, can modify the stability region in applied fields. The skyrmions are observed in $SrRuO_3$ at rather high temperatures (T$\sim$ 70 K), which bears a resemblance to high-T skyrmions observed near the critical temperature in bulk B20 compounds found in a narrow T-H window [36]. Additionally, the origin of hump features was ascribed to two-channel anomalous Hall effect without employing the effect of skyrmions [77–80]. Despite remarkable progress, the role of itinerant magnetism remains not fully understood in these materials. The resulting hump features are likely a combination of effects from the real and reciprocal space non-trivial topology [81, 82], being highly dependent on the film growth conditions and structural inhomogeneities, which is discussed in great detail in a recent review [83]. Several methods to distinguish the Topological Hall Effect from Anomalous Hall Effect have been recently proposed [84].

$SrRuO_3$ gives fertile grounds to study electric manipulation of magnetic order, e.g., as for recently discussed topological Hall torque in this material [85]. Future spintronics applications can benefit from a tailored interplay between magnetocrystalline anisotropy, long-range magnetodipolar forces, and the interfacial Dzyaloshinskii-Moriya interaction using the skyrmions properties to manipulate information.

2.6 Appendix

2.6.1 Numerical simulations

The energy of the magnetic bubble array phase is found by numerical minimization of the total energy Eq. (2.1) with respect to the Fourier harmonics of the magnetization,

$\tilde{\boldsymbol{M}}(\boldsymbol{q})$, where the wave vector $\boldsymbol{q}$ belongs to the reciprocal lattice of the array with the basis vectors, $\boldsymbol{b}_1^* = \frac{2}{\sqrt{3}a}(1,0)$ and $\boldsymbol{b}_2^* = \frac{2}{\sqrt{3}a}(-\frac{1}{2}, \frac{\sqrt{3}}{2})$, a being the lattice constant of the bubble crystal, an additional parameter with respect to which the energy is minimized. We limit the number of the Fourier harmonics by $q \leq 4b_1^*$ (61 harmonics in total, see Fig. 2.2d) and do checks for larger wave vectors sets to ensure that the contribution of the neglected harmonics is small. A similar procedure is applied to study the stripe domain state, in which case all wave vectors are collinear. The number of harmonics is large enough to simulate spin textures of all competing phases as well as their deformations in a tilted magnetic field. This energy minimization method is introduced in Sec. 1.6.3.

To obtain phase diagrams shown in Figs. 2.3 and 2.5, we performed simulations for $h = 8.9$ nm, the saturation magnetization $M_\mathrm{s} = 3\mu_\mathrm{B}$ per Ru ion [63] and the spin stiffness constant, $A = V_\mathrm{Ru} M_\mathrm{s}^2 c = 62$ meV·Å^2, taken from neutron scattering data on bulk SRO [76] (V_Ru is the volume per Ru ion). Distances are measured in units of h and energy is given in units of $V_\mathrm{Ru} M_\mathrm{s}^2$=0.008 meV. The dimensionless DM constant, $D = 1$, used to calculate the spin configurations shown in Fig. 2.2 c,d and the phase diagrams Fig. 2.3 c,d correspond to the Dzyaloshinskii-Moriya interaction $D_\mathrm{nn} = 0.8$ meV between nearest-neighbor spins of the uppermost layer, which can be compared with the nearest-neighbor Heisenberg exchange constant $J_\mathrm{nn} = 6.2$ meV in a discrete spin model that gives the experimental value of the stiffness constant A.

The dimensionless energy is

$$\begin{aligned}\tilde{E} = \left(\frac{h^3}{V_\mathrm{Ru}}\right) \int d^2\tilde{x} \Big[\sum_{i=x,y} \frac{\tilde{c}}{2} (\partial_i \boldsymbol{m})^2 - \frac{K_1}{2} m_z^2 - \frac{K_2}{4} m_z^4 \\ - \boldsymbol{h} \cdot \boldsymbol{m} + \frac{\lambda}{4} \left(\boldsymbol{m}^2 - 1\right)^2 \Big] + \tilde{E}_\mathrm{ms},\end{aligned} \tag{2.7}$$

with tilde providing dimensionless units: the energy $\tilde{E} = \frac{E}{V_\mathrm{Ru} M_\mathrm{s}^2}$, distance $\tilde{x} = \frac{x}{h}$, exchange constant $\tilde{c} = \frac{c}{h^2}$, magnetization $\boldsymbol{m} = \frac{\boldsymbol{M}}{M_\mathrm{s}}$ and field $\boldsymbol{h} = \frac{\boldsymbol{H}}{M_\mathrm{s}}$.

2.6.2 Variational bubble solution

Single parameter Ansatz

Here we discuss variational solutions for an isolated magnetic bubble Eq (2.2). We first consider the case of $\epsilon = \frac{1}{2}$,

$$1 - m_z(r) = \frac{2}{\left(1 + \left(\frac{r}{a}\right)^2\right)^{3/2}}. \tag{2.8}$$

The magnetostatic energy of the bubble counted from uniform state,

$$E_{\text{uniform}} = hSM_{\text{s}}^2 \left(-\frac{K_1}{2} + \frac{K_2}{4} - \frac{H}{M_{\text{s}}} + 2\pi \right), \tag{2.9}$$

is

$$E_{\text{ms}} = 2\pi hSM_{\text{s}}^2 \left(\sum_{\boldsymbol{q}} f(qh)|m_{\boldsymbol{q}}^z|^2 - 1 \right), \tag{2.10}$$

where $m_{\boldsymbol{q}}^z = \frac{1}{S}\int d^2x\, e^{-i\boldsymbol{q}\cdot\boldsymbol{x}} \cos\theta(\boldsymbol{r}) = \delta_{\boldsymbol{q},0} - \frac{2\pi}{S}\tilde{g}_{\boldsymbol{q}}$ with

$$\tilde{g}_{\boldsymbol{q}} = \int \frac{d^2x}{2\pi}\, e^{-i\boldsymbol{q}\cdot\boldsymbol{x}} \left(1 - \cos\theta(\boldsymbol{r})\right) = \int_0^\infty rdr\ \left(1 - \cos\theta(\boldsymbol{r})\right) J_0(qr), \tag{2.11}$$

and the integration over the azimuthal angle φ was performed using

$$e^{i\boldsymbol{q}\boldsymbol{x}} = \sum_{n=-\infty}^{+\infty} iJ_0(qr)e^{in(\varphi-\varphi_{\boldsymbol{q}})}, \tag{2.12}$$

where $J_0(x)$ is the Bessel function of the first kind. This leads to the magnetostatic energy,

$$E_{\text{ms}} = 2\pi hM_{\text{s}}^2 \left(-4\pi\tilde{g}_{q=0} + \int d^2q\, f(qh)|\tilde{g}_{\boldsymbol{q}}|^2 \right). \tag{2.13}$$

Integration over r is Eq (2.11) gives (see [86]) $\tilde{g}_q = 2a^2e^{-qa}$. Performing integration over q in the last equation, we obtain

$$E_{\text{ms}} = -\frac{\pi^2 M_{\text{s}}^2 d^2 h}{d+h}\left(3d + 4h\right), \tag{2.14}$$

with $d = 2a$. Other energy terms can be calculated directly, e.g., using the substitution: $z = \frac{a}{\sqrt{a^2+r^2}}$. In this way we obtain Eq (2.3) for the energy given in the main text. The size-dependent part of the energy is

$$\Delta E_{\text{bubble}} \sim d^2 \left(D - \frac{h}{d+h} \right), \tag{2.15}$$

with $D = 3(Q-1) - \frac{87}{140\pi}K_2 + \frac{H}{\pi M_{\text{s}}}$. Minimization of the bubble energy with respect to the bubble diameter, d, gives

$$x^2 + x - 2D = 0, \tag{2.16}$$

where $x = \frac{h}{h+d}$. The condition for $d > 0$ is $D \leq 1$ and the critical fields ($D = 1$). Inserting the optimal variational solution into Eq (2.3), we obtain the bubble energy,

$$E_{\text{bubble}} = I\pi cM_{\text{s}}^2 h - \pi^2 M_{\text{s}}^2 h^3 \frac{(1-x)^2(x-D)^2}{x^2}, \tag{2.17}$$

where the first term is the d-independent exchange energy with $I = 4.0495$

Two parameter Ansatz

The Zeeman and single-ion anisotropy energies for arbitrary ϵ are given by

$$\int d^2x \, (1 - m_z) = \frac{2\pi a^2}{\epsilon}, \tag{2.18}$$

$$\int d^2x \, \left(1 - m_z^2\right) = 4\pi a^2 \left(\frac{1}{\epsilon} - \frac{1}{1+2\epsilon}\right), \tag{2.19}$$

$$\int d^2x \, \left(1 - m_z^4\right) = 8\pi a^2 \left(\frac{1}{\epsilon} - \frac{3}{1+2\epsilon} + \frac{4}{2+3\epsilon} - \frac{2}{3+4\epsilon}\right). \tag{2.20}$$

the exchange energy

$$E_{\text{ex}} = c\pi M_{\text{s}}^2 h \int_0^\infty r dr \, \left(\left(\frac{d\theta}{dr}\right)^2 + \frac{\sin^2\theta}{r^2}\right), \tag{2.21}$$

can be calculated using the substitution $\frac{r}{a} = e^t$, so that

$$z = \frac{(1 - \cos\theta)}{2} = \frac{1}{\left(e^{2t} + 1\right)^{1+\epsilon}}, \tag{2.22}$$

$$\frac{1}{2} \int_{-\infty}^{\infty} dt \, \left(\frac{d\theta}{dt}\right)^2 = (1+\epsilon) \int_0^1 dz \, \frac{1 - z^{\frac{1}{1+\epsilon}}}{1-z}, \tag{2.23}$$

and

$$\frac{1}{2} \int_{-\infty}^{\infty} dt \, \sin^2\theta = \frac{1}{1+\epsilon} \int_0^1 dz \, \frac{1-z}{1 - z^{\frac{1}{1+\epsilon}}}. \tag{2.24}$$

The magnetostatic energy is calculated using (cf. Eq (2.11))

$$\tilde{g}(q, \epsilon) = 2a^2 \left(\frac{qa}{2}\right)^\epsilon \frac{K_\epsilon(qa)}{\Gamma(1+\epsilon)}. \tag{2.25}$$

Using these results, we numerically calculate the remaining integrals and minimize the total bubble energy with respect to the variational parameters a and ϵ.